Study of β-delayed particle emission: The cases of ^{11}Be and ^{20}Mg

Supervisor: Hans Otto Uldall Fynbo

Progress Report

Morten Vinther Lund

January 1, 2014

Department of Physics and Astronomy
Aarhus University

Preface

This progress report describes the main work I have performed during the first two years of my Ph.D. study. I have spent most of my time analyzing data from two experiments performed at ISOLDE, CERN, both of which I have participated in.

The first experiment is a beta-decay study of ^{20}Mg performed in November 2011 a few months before I started my Ph.D. At this time I was already familiar with the ISOLDE facility due to my participation in the CERN summer student school 2011.

The second experiment is a beta-decay study of ^{11}Be with a first attempt in July 2012, which was unsuccessful, due to target problems at ISOLDE. The second attempt in December 2012 was successful. I have participated in both experiments.

Besides analyzing data from these two beta-decay experiments, I have participated in several other experiments at ISOLDE, CERN, and KVI, Groningen, and attended several nuclear physics schools. A complete list is presented below. I also used some time working with the groups experiments located in the basement of the department in Aarhus.

Finally I am a co-author of two submitted papers both mentioned below.

Experiments:

- Experiment IS507, ISOLDE, CERN: Study of the β-decay of ^{20}Mg. November 2011.
- Experiment IS541, ISOLDE, CERN: Search for beta-delayed protons from ^{11}Be. (Unsuccessful). July 2012.
- Experiment IS505, ISOLDE, CERN: Study of the deuteron emission in the β decay of ^{6}He. August 2012.
- Experiment P20, KVI, Groningen: β-delayed α-decay study of ^{16}N using the implantation method (test experiment). October 2012.
- Experiment IS445 and IS476, ISOLDE, CERN: Experiments with the newly available Carbon beams at ISOLDE (yield test) and Studies of β-delayed two-proton emission: The cases of ^{31}Ar and ^{35}Ca. November 2012.
- Experiment IS541, ISOLDE, CERN: Search for beta-delayed protons from ^{11}Be. December 2012.
- Experiment P20, KVI, Groningen: β-delayed α-decay study of ^{16}N using the implantation method. May 2013.

Participation in schools and workshops:

- Euroschool on Exotic Beams, Athens, Greece. August 2012.
- 10th Russbach Workshop on Nuclear Astrophysics, Austria. March 2013.
- Euroschool on Exotic Beams, Dubna, Russia. August 2013.
- Shell Model Course for Non-Practitioners, CERN. October 2013.
- ISOLDE workshop and users meeting, CERN. November 2013.

Publications. The following papers has been submitted for publication:

- J.P. Ramos, A. Gottberg, T.M. Mendonça, C. Seiffert, H.O.U. Fynbo, O. Tengblad, J.A. Briz, M.V. Lund, G.T. Koldste, M. Carmona-Gallardo, V. Pesudo, A.M.R. Senos, T. Stora, *Intense* $^{31-35}$*Ar beams produced with a nanostructured CaO target at ISOLDE*, submitted to Nuclear Inst. and Methods in Physics Research, B.
- K. Riisager, O. Forstner, M.J.G. Borge, J.A. Briz, M. Carmona-Gallardo, L.M. Fraile, H.O.U. Fynbo, T. Giles, A. Gottberg, A. Heinz, J.G. Johansen, B. Jonson, J. Kurcewicz, M.V. Lund, T. Nilsson, G. Nyman, E. Rapisarda, P. Steier, O. Tengblad, R. Thies, S.R. Winkler, *Quasi-free neutron decay in the periphery of a nucleus*, submitted to Nature Physics.

Contents

1

Motivation

The first model describing the existence of the atomic nucleus was Rutherford's model of the atom published in 1911, see [1]. Rutherford was investigating the structure of the atom by aiming a beam of alpha-particles with a fixed kinetic energy at a stationary foil of gold. By measuring the outcome of the scattering process - i.e. which particles emerged in which directions and with what energy - Rutherford determined that the atom consists of a centrally placed nucleus containing all mass and charge and with a radius smaller than at least $30 \cdot 10^{-15}$m. As the atomic radius is about 10^{-10}m, the atomic nucleus must be at least four orders of magnitude smaller. The conclusion is that the electrons of the atom are orbiting a much smaller nucleus, which has almost all the mass of the atom and a positive charge exactly equal in magnitude to that of all the electrons.

The main objective of nuclear physics is to study this atomic nucleus, which consist of protons and neutrons, in general called nucleons. The nucleons are held together by the nuclear force, which together with quantum mechanics is responsible for the structure of the nucleus. The investigation and understanding of the structure of the nucleus was a key step in order to infer the underlying physics of the nuclear force.

The structure of the nucleus is completely described by the total nuclear wave function and the nuclear properties can be calculated as expectation values of the quantum mechanical operators. However, the nucleus is in most cases far too complex to compute the complete wave function, and the exact form of the nuclear force is also not known because the fundamental force between the quarks, QCD, is strong at the energy scale relevant for nuclei.

The way to proceed in order to make theoretical predictions of the properties of the nucleus is to model the system based on a few fundamental assumptions. This approach has lead to several interesting models of the nucleus, like the liquid drop model and the independent particle model (IPM). The liquid drop model assumes that the nucleus is a uniform sphere of nuclear matter, which is equivalent to an incompressible liquid droplet. In 1935 Weizsäcker developed the Semi-Empirical Mass Formula on the basis of the liquid drop model, which describes the general trend of the binding energy quite well.

The IPM go to the other extreme and assume that the nucleons are moving around independently in an effective overall potential describing the interaction with all other nucleons. The effective potential could be that of a harmonic oscillator and filling the energy levels with nucleons according to the Pauli exclusion principle leads to the structure of the nucleus. Including a strong spin-orbit coupling in the effective potential, the model successfully reproduces the magic numbers describing particular strongly bound nuclei, which the liquid drop model fails to predict.

The best description of the actual structure of the nucleus will often be somewhere in between the two extreme assumptions, making it a mixture of clustering states and single particle states. Sometimes the nucleus gains energy by organizing itself in clusters like the α-particle or even heavier clusters.

A halo structure is an expression of clustering in the nucleus and is defined as a spatially extended object measured in terms of the natural length scale of the system, which could be

the range of the potential or the spatial radius of nuclei with a similar mass. The spatial extension of some light halo nuclei is as large as that of Lead because the wavefunction of the halo nucleon has a small amplitude at the center of the nucleus but extends out to very large distances. This kind of structure is possible in nuclei with a very small separation energy of the least bound nucleon.

In modern theoretical nuclear physics the modeling of the nuclear structure is approached from a more fundamental level in ab-initio calculations, which calculates the structure of the nucleus directly from the first principles of quantum mechanics, without using any measured properties as input parameters. Using an interaction deriving from QCD it is possible to reproduce the structure and properties of the low-mass nuclei rather well in e.g. no-core shell models, [2]. However, the calculations requires a large number of numerical computations, which limits the precision for heavier nuclei and the possibility of using higher-order interactions like three- and four-body forces.

1.1 The one-neutron halo nucleus ^{11}Be

^{11}Be is a light nucleus located close to the neutron dripline and is known for being a one-neutron halo nucleus [8]. It decays by beta-decay to ^{11}B with a half-life of 13.81(8) seconds, which is an unusual long half-life compared to other halo nuclei. In very rare cases it may decay by beta-delayed proton emission, though it may seem counterintuitive for a nucleus close to the neutron dripline to emit protons. However, this decay mode is energetically allowed precisely because the neutron separation energy is so low in ^{11}Be, see [6]. This very rare decay mode is believed to proceed as a decay of the halo neutron directly into a continuum proton ([7]), which will provide a new and independent probe of the single neutron halo structure.

It is expected that due to the relative long half-life of ^{11}Be the branching ratio will be larger by several orders of magnitude compared to other one-neutron halo nuclei. This makes ^{11}Be the optimal case to study. Indeed various theoretical models have predicted the branching ratio to be between a few times 10^{-8} and up to above 10^{-6}. A recent sophisticated calculation with a two-body potential model predicts a branching ratio of $3.0 \cdot 10^{-8}$ with a broad energy spectrum peaking at 0.1-0.2 MeV ([7]). Together with low energy alpha particles from the decay, this will make the protons very difficult to identify directly.

1.2 Study of ^{20}Mg beta-decay

The motivation for studying the beta-decay of ^{20}Mg is three-fold with both nuclear physics and stellar evolution perspectives. The nuclear physics motivation is to study the almost complete charge independence of the nuclear force. This is possible to do by comparing the $\log_{10}(ft)$ values of isospin mirrored beta-decays, which should be equal if the nuclear force really is charge independent. However, in general an asymmetry is observed. The mirror beta-decay of ^{20}Mg is the beta-decay of ^{20}O to ^{20}F.

The second motivation is to compare the decay with modern Shell-Model calculations. As ^{20}Mg is the lightest $T = 2$ nucleus the decay properties can be reliably calculated with modern Shell-Model calculations (see [4]), and it is therefore a good testing ground of the Shell-Model.

The last motivation has to do with energy production in stars, more precisely in explosive environments, which is governed by fusion of light nuclei generally starting with the reaction with the lowest Coulomb barrier. The stellar evolution is quite sensitive to the exact reaction rates, making it important to measure the relevant nuclear physics properties.

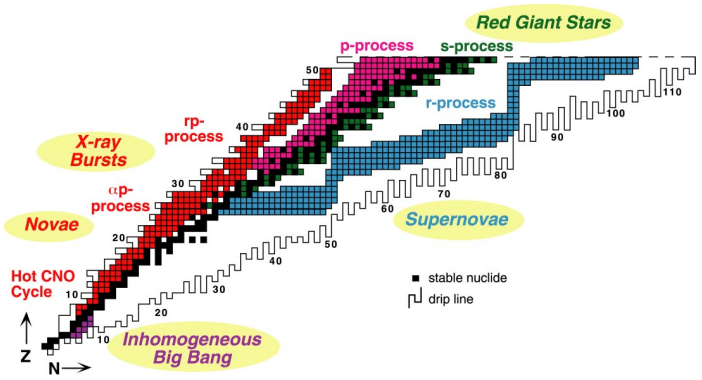

Figure 1.1: *The nuclear landscape in terms of stellar nucleosynthesis. The HCNO cycle and breakout from HCNO is located close to or at the proton dripline in explosive environments, respectively novae and x-ray bursts. Figure from [3]*

Explosive hydrogen burning and breakout of the HCNO cycles

Typical places for explosive hydrogen burning are classical novae's and type I X-ray bursts. A classical novae is a thermonuclear runaway caused by accretion of material rich in hydrogen and helium from a large main-sequence star onto the surface of a white dwarf in a close binary system. A type I X-ray burst is fueled by accretion of hydrogen- and helium-rich matter onto the surface of a neutron star with a strong magnetic field in a close binary system with a population I star with $M \geq 5M_{\odot}$. The type I X-ray bursts are the most frequent type of thermonuclear stellar explosion in the galaxy.

In both cases the hot CNO (HCNO) cycles will dominate the energy production by turning hydrogen into helium when the temperature of the accreted matter reaches $T = 0.1 - 0.4$ GK. The HCNO cycles are essentially closed and happens in the $A = 12 - 18$ region, [23]. For novae the end point of nucleosynthesis will be at $A \approx 40$. The heavy elements, however, are not generated by breakout from the HCNO cycles but through the presence of heavy seed nuclei in the white dwarf, [5].

For type-I X-ray bursts the temperature rises to $T > 0.4$ GK and new reactions start to compete with some of the reactions in the HCNO cycles. This opens the possibility for transferring material from the $A = 12 - 18$ region and into the $A = 20 - 21$ region and beyond. The nuclei converted in this breakout are essentially lost for the HCNO cycles. Three breakout sequences from the HCNO cycles exist,

$$^{15}\mathrm{O}(\alpha,\gamma)^{19}\mathrm{Ne}(\mathrm{p},\gamma)^{20}\mathrm{Na} \tag{1.1}$$

$$^{14}\mathrm{O}(\alpha,\mathrm{p})^{17}\mathrm{F}(\mathrm{p},\gamma)^{18}\mathrm{Ne}(\alpha,\mathrm{p})^{21}\mathrm{Na} \tag{1.2}$$

$$^{14}\mathrm{O}(\alpha,\mathrm{p})^{17}\mathrm{F}(\gamma,\mathrm{p})^{16}\mathrm{O}(\alpha,\gamma)^{20}\mathrm{Ne} \tag{1.3}$$

After breakout the energy production continues by alpha and proton captures on the heavier and heavier nuclei produced by the αp- ($A \leq 30$) and rp-processes ($A \geq 33$) as shown on Figure 1.1. The end point for nucleosynthesis in type I X-ray bursts are at $A \approx 100$ by the rp-process. The reactions runs along the proton dripline and are very sensitive to both the exact position of the proton dripline but also to photo disintegration.

Spin and parity of the 2.645(6)MeV resonance in ^{20}Na

As is seen in equation (1.1) the first of the three breakout sequences goes through ^{20}Na by proton capture on ^{19}Ne. The level at 2.645(6)MeV in ^{20}Na, see Figure 1.2, is located in the

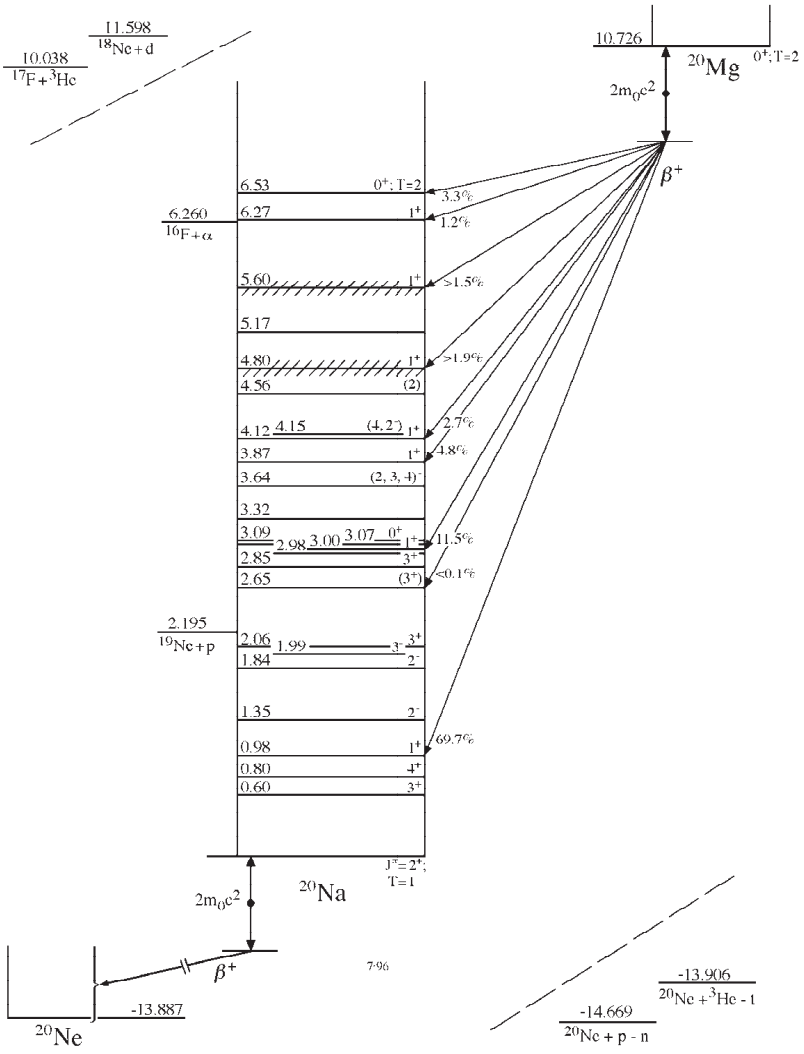

Figure 1.2: *Decay scheme for allowed beta-decay of* ^{20}*Mg populating* 1^+ *states in* ^{20}*Na. Taken from [4].*

Gamow-window of the ^{19}Ne(p, γ)^{20}Na reaction and is therefore decisive for the reaction rate. The spin and parity of this level is not yet fully determined, but the most likely values are 1^+ or 3^+ as seen by comparing to the mirror nucleus. In the former case, the resonance can be populated in allowed beta-decay of ^{20}Mg. A 3^+ assignment makes it a second-forbidden transition, which greatly suppresses the beta feeding of the resonance.

A recent measurement of the beta-decay of ^{20}Mg with a half-life of 90.8(24)ms, set an upper limit on the beta-decay branch to this level of 0.02%, see [10]. This low beta-decay branching favors the 3^+ assignment but does not completely rule out the 1^+ possibility.[1]

[1]See the section on beta-decay theory in the next chapter.

2

The experimental approach

For both nuclei studied, ^{20}Mg and ^{11}Be, the ISOLDE facility at CERN was used to produce a clean radioactive ion beam containing mainly the desired nuclei. The beam will have a small degree of contamination from isobars, but the contamination will be suppressed due to the high degree of selectivity in the ionization process and the use of the ISOLDE High Resolution Separator (HRS), a magnetic mass separator.

In this chapter some basic theory of beta-decays will be presented. Next comes a short introduction to the ISOLDE facility, with a short general description of the most important working principles. Then the experimental setup for the ^{11}Be and ^{20}Mg experiments will be presented in turn.

2.1 Beta-decay theory

The nuclei on both sides of the valley of stability are unstable and decay weakly by beta-decay towards stability. On the neutron rich side of stability the nuclei decays by β^--decay,

$$n \rightarrow p + e^- + \bar{\nu}_e \tag{2.1}$$

On the proton rich side of stability they decays by β^+-decay or electron capture,

$$p \rightarrow n + e^+ + \nu_e \tag{2.2}$$

$$p + e^- \rightarrow n + \nu_e \tag{2.3}$$

Moving away from stability the isobaric mass difference increase parabolically, making the Q-value larger and the life-time shorter. As the ground state to ground state Q-value gets larger, more and more excited states may be populated in the beta-decay. Taking advantage of the selection rules for beta-decay makes it a good way of studying specific excited states in the daughter.

Fermi and Gamow-Teller decays

Beta-decay is a weak interaction process with an effective interaction operator, which is constituted of a vector and an axial-vector part. The two parts have separate transition operators giving rise to two different beta-decay modes, i.e. Fermi and Gamow-Teller decays. In Fermi decays the lepton spins are antiparallel, so the total leptonic spin couple to $\vec{S_L} = \vec{0}$. In the case of Gamow-Teller decays the lepton spins are parallel, so the combined system of neutrino and charged lepton have $\vec{S_L} = \vec{1}$.

Looking at the matrix element for the transition, it can be written as

$$M_{fi} = \int [\psi_f^* \psi_e^* \psi_\nu^*] H \psi_i \mathrm{d}V, \tag{2.4}$$

where ψ_f and ψ_i are the initial and final nuclear wavefunctions and H is the Hamiltonian of the effective interaction. Using the fact that the leptons' Dirac spinors are proportional to a normalized plane wave (times a 4-component spin function), see [12], the matrix element can be simplified using an expansion of the plane wave,

$$e^{i\vec{p}\cdot\vec{r}/\hbar} \approx \left(1 + i\vec{p}\cdot\vec{r}/\hbar - \frac{1}{2}(\vec{p}\cdot\vec{r}/\hbar)^2 + ...\right) \tag{2.5}$$

As the nuclear wavefunctions restrict the spatial integration of the matrix element to the nuclear volume, the plane waves are well approximated by the constant term as long as $pR/\hbar \ll 1$ (where R is the nuclear radius). For an electron with a normal energy of 1MeV, $p = 1.4\text{MeV/c}$ and $p/\hbar = 0.007\text{fm}^{-1}$, which makes it a good approximation. The approximation leads to the following expression for the comparative half-life ([12]),

$$ft_{1/2} = \frac{4\pi^3(\hbar c)^6\hbar \ln 2}{G_F^2(m_e c^2)^5} \cdot \frac{1}{|M_{fi}|^2} \tag{2.6}$$

where f is a dimensionless function proportional to the decay rate $\omega = \ln 2/t_{1/2}$.

Sometimes it is necessary to keep higher order terms in the expansion to get a matrix element different from zero, i.e. to get a finite lifetime. The procedure is to include terms in the expansion until a non-zero matrix element is reached. The transitions obtained are classified as allowed, first-forbidden, second-forbidden, and so on according to the number of terms included. For each additional term included the matrix element contains an extra factor of $pR/\hbar$, which depending on nucleus and beta-particle energy, typically is about 10^{-2}, see [12]. Thus the $\log_{10}(ft_{1/2})$ values increase by a rough factor of 4 for each additional degree of forbiddenness, making it less and less likely.

Selection rules

Beta-decays conserves the total angular momentum, so

$$\vec{J_i} = \vec{J_f} + \vec{J_L} \tag{2.7}$$

where $\vec{J_i}$ is the initial nuclear angular momentum, $\vec{J_f}$ is the final nuclear angular momentum, and $\vec{J_L} = \vec{L_L} + \vec{S_L}$ is the total leptonic angular momentum. Following the rules of addition of angular momentum, it is clear that

$$J_i = |J_f - J_L|, ..., J_f + J_L \tag{2.8}$$

are the possible values of J_i given J_f and J_L.

The degree of forbiddenness in beta-decays may be translated to the value of the total leptonic orbital angular momentum $\vec{L_L}$. For allowed decays the lepton wavefunctions are constants making $\vec{L_L} = \vec{0}$, and for forbidden decays the lepton wavefunctions will depend on the coordinate $\vec{r}$ of the lepton giving rise to $\vec{L_L} = \vec{1}$ for first-forbidden, $\vec{L_L} = \vec{2}$ for second-forbidden, and so forth.

Defining $\Delta J \equiv |J_i - J_f|$ it follows for allowed transitions that,

$$\begin{aligned} \Delta J = 0,\ \Delta P = 1 \quad &\text{(Fermi transition)} \\ \Delta J = 0, 1,\ \Delta P = 1 \quad &\text{(Gamow-Teller transition)} \end{aligned}$$

For Gamow-Teller transitions a $0^+ \to 0^+$ transition is not allowed, since the leptons will carry away one unit of angular momentum ($\vec{J_L} = \vec{1}$).

For first-forbidden transitions the selection rules are,

$$\Delta J = 0, 1,\ \Delta P = -1 \quad \text{(Fermi transition)}$$
$$\Delta J = 0, 1, 2,\ \Delta P = -1 \quad \text{(Gamow-Teller transition)}$$

For second-forbidden transitions the selection rules are,

$$\Delta J = 1, 2,\ \Delta P = 1 \quad \text{(Fermi transition)}$$
$$\Delta J = 1, 2, 3,\ \Delta P = 1 \quad \text{(Gamow-Teller transition)}$$

In principle the Fermi case allows for $\Delta J = 0$ here, but it is exactly the same as for allowed Fermi transitions, and the allowed decay will dominate.

Beta-delayed particle emission

Moving away from stability the isobaric mass differences will increase parabolically, and at the same time the separation energy of the least bound nucleon will get closer to zero. This makes it increasingly probable that the beta-decay will populate particle unbound states in the daughter. If a beta-decay is followed by particle emission from the daughter, the decay mode is referred to as beta-delayed particle emission. Measuring the emitted charged particles makes it possible to determine properties of the unbound resonances.

2.2 Production of exotic nuclei at ISOLDE

The ISOLDE facility at CERN, see Figure 2.1, is consuming roughly half of the protons accelerated by the CERN accelerator complex. The protons are accelerated in bunches with a spacing between adjacent bunches of 1.2 seconds in the overall super-cycle. The energy of the protons are 1.4 GeV.

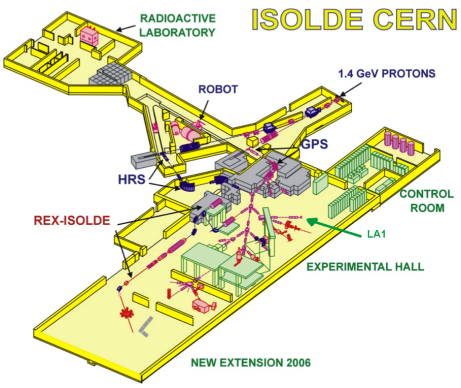

Figure 2.1: *Sketch of the ISOLDE facility at CERN showing the target area behind the concrete blocks (grey colors), the HRS mass separator, and the LA1 beam line in the experimental hall among other things.*

When the protons bombard the target of a heavy material they induce spallation, fragmentation, and fission. All of these processes will produce lighter nuclei than the target material. In the case of ^{20}Mg the target is SiC, and for the production of ^{11}Be it is UC_x. The target material is carefully chosen such as to produce the largest possible yield of the isotope of interest.

The produced fragments are extracted from the target and moved into an ion source. The ionization is done with the Resonant Ionization Laser Ion Source (RILIS), [11]. The

technique of RILIS takes advantage of the interaction between the nuclei and the surrounding electrons, which results in the hyperfine structure of the atom. It is well known that the hyperfine structure splitting depends on the isotope in question, and hence can be used to select a specific isotope for ionization.

As ionization also happens by surface ionization or dissociation, it is not guaranteed that only the isotope of interest is ionized. Usually there will be significant fractions of other unwanted components in the beam. However, by using a magnetic mass separator it is possible to suppress this contamination with several orders of magnitude. For both experiments the HRS were used, producing a clean beam delivered at 60 keV to the experimental setup at LA1, see Figure 2.1.

2.3 The experimental setup for ^{11}Be collection

The aim of the experiment is to measure the branching ratio for beta-delayed proton emission from ^{11}Be with a half-life of 13.81(8) s to the daughter nucleus ^{10}Be, which has a half-life of 1.387(12) $\times 10^6$ y making it practically stable. At ISOLDE a very clean sample of ^{11}Be atoms was collected in a pure Cu plate by use of RILIS and the HRS mass separator. After the ISOLDE beam time the Cu plate was send to the University of Vienna for examination at the VERA facility - an Atomic Mass Spectrometry (AMS) facility - to get the number of ^{10}Be atoms in the Cu plate. This measurement was performed a few months after the collection, which was possible due to the large difference in half-lives of the parent and daughter nucleus. The ratio of the number of ^{10}Be atoms to the number of ^{11}Be atoms gives the desired branching ratio.

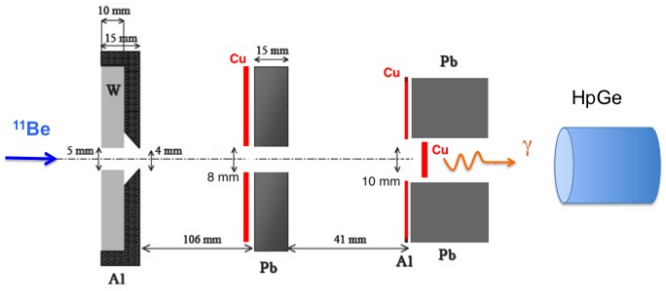

Figure 2.2: *Sketch of experimental setup for collection of ^{11}Be. Starting from the left side of the picture the beam of ^{11}Be enters the detection chamber through a small collimator. Then it passes two more collimators each with a Cu piece in front to measure the current before the beam finally is implanted in the Cu plate itself. Outside the chamber with lead shielding in front (not shown) a standard Canberra HPGe-detector cooled with liquid nitrogen measures the gamma-rays emitted. Figure copied from [8].*

During the implantation of ^{11}Be in the Cu plate the HPGe-detector was measuring the gamma-rays emitted from excited states in ^{11}B populated in the beta-decay of ^{11}Be (see the decay scheme on Figure 2.3). In order to determine how many atoms were collected in the Cu plate the 2124 keV gamma-ray with $b_\gamma = 0.355 \pm 0.018$ and the 2895 keV gamma-ray with $b_\gamma = (0.355 \pm 0.018) \cdot (2.27 \pm 0.08) \cdot 10^{-3} = (8.06 \pm 0.50) \cdot 10^{-4}$ were used. The gamma-ray intensities quoted includes feeding from higher levels, see [15]. A detailed sketch of the experimental setup at the end of the LA1 beam line at ISOLDE is shown on Figure 2.2. As is described in the caption the three collimators are enclosed in a standard vacuum chamber and between the Cu plate and the HPGe-detector outside the chamber is a block of lead located in order to lower the count rate and hence the dead time of the HPGe-detector.

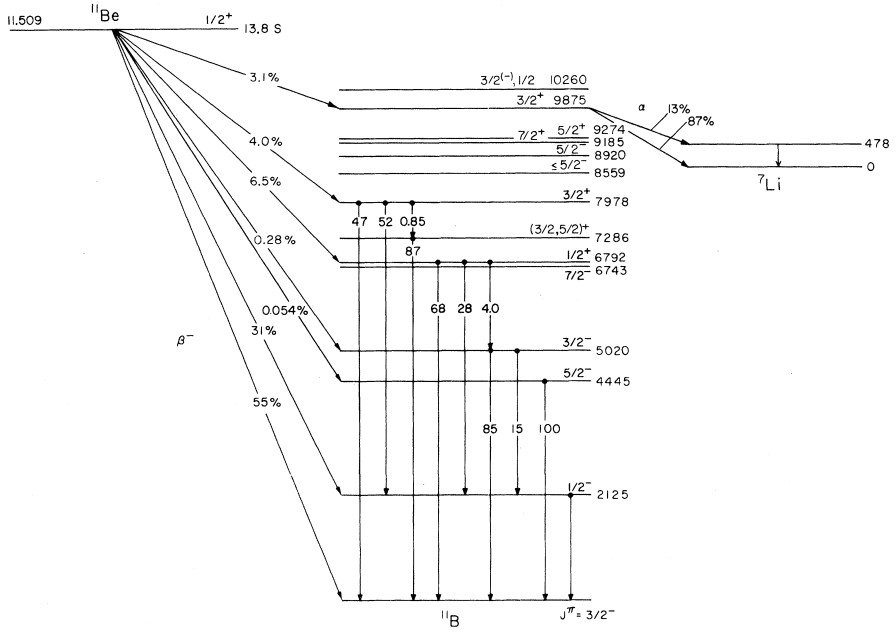

Figure 2.3: *Decay scheme of the ^{11}Be beta-decay. ^{11}Be beta-decays to the ground state or excited states in ^{11}B. When the excited states are populated, which happens in 45% of the decays, gamma-rays are emitted when ^{11}B de-exites to the ground state. In very rare cases the beta-decay might be followed by proton emission resulting in the production of ^{10}Be instead of ^{11}B.*

2.4 The experimental setup for the β-decay study of ^{20}Mg

To make a detailed study of the beta-decay of ^{20}Mg a small dedicated setup at LA1 at ISOLDE was used. It is important to be able to do particle identification, which can be done in a elegant manner by the $\Delta E - E$ technique, several charged particle detectors were used, see Figure 2.4.

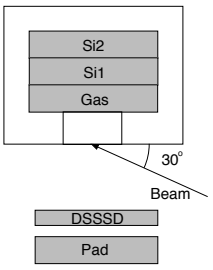

Figure 2.4: *Sketch of experimental setup for beta-decay study of ^{20}Mg (not to scale). The beam is implanted in the window (where arrow ends) of a gas telescope detector. Directly opposite is a $61\mu m$ thin Double Sided Silicon Strip Detector (DSSSD), which is backed by a $1000\mu m$ Si detector, both with an area of 5×5 cm^2. The distance from the gas window to the DSSSD is about 44 mm. The areas of Si1 and Si2 are 300 mm^2 and they are respectively 300 μm and 500 μm thick but both are mounted in a holder that is 7.9 mm thick (shaded region named Si1/Si2), the same thickness as the active gas (shaded region named gas).*

3

Analysis and results: ^{11}Be

In this chapter follows a description of the analysis of the ^{11}Be beta-decay experiment with the aim of measuring the branching ratio of beta-delayed proton emission with the daughter nucleus ^{10}Be. In the first section is the energy calibration of the HPGe-detector presented. The second section is a description of the efficiency calibration of the detector. It is needed in order to know the fraction of the emitted gamma-rays seen by the HPGe-detector. Then follows a section on the estimation of the number of ^{11}Be atoms collected in the Cu plate by use of the efficiency calibration. In section four is a discussion of the possible beam background, i.e. how many of the measured ^{10}Be atoms could potentially originate from other components in the beam than ^{11}Be. Finally everything is combined to get the branching ratio for beta-delayed proton emission.

3.1 Energy calibration of the HPGe-detector

The HPGe-detector needs to be energy calibrated to identify the various gamma-rays emitted. It is calibrated by measuring sources with known gamma-ray energies. The three different sources used were ^{60}Co, ^{152}Eu, and ^{228}Th (see Table 3.3 for the literature energies). A fit with a standard Gaussian distribution was performed, in order to get the centroid channel number of the gamma lines. Using the uncertainty given by the fit on the centroid value and the uncertainty on the literature energy, a linear fit to the channel number versus literature energy was made. The resulting gain and offset can be seen in Table 3.1.

Table 3.1: *Parameters from the energy calibration for specific data files.*

File number	Gain (keV/channel)	Offset (keV)
1−6	No calibration performed	
7−11	0.89860(3)	−82.22(3)
12−19	1.10172(5)	−101.611(61)
20−23	Not possible to calibrate.[a]	
24−34	1.10598(5)	−102.357(62)
35−41.4[b]	1.10465(6)	−102.994(113)
41.4−43[c]	Not possible to calibrate.[d]	
44−59	1.00314(5)	−96.4839(638)
60−68	1.02224(9)	−98.096(113)

[a] Continuous shift of the 511 keV line.
[b] This calibration is done using the ^{11}Be energy spectrum.
[c] No calibration performed due to the simple ^{11}Be energy spectrum without the high-energy lines.
[d] 511 line jumps by roughly a factor of 2 during run 41 file 4. After run 43 the gain is manually changed on the amps.

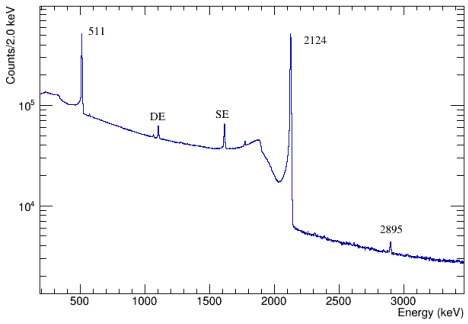

Figure 3.1: *Decay spectrum of ^{11}Be measured with the HPGe-detector. The 2124 keV gamma-ray and the Single and Double Escape (SE and DE) lines are clearly seen. The 2895 keV gamma-ray is also visible.*

During the experiment it was noticed that the amplification of the HPGe-detector suddenly changed by approximately a factor of 2, most likely due to a broken amplifier. The effect of the broken amplifier on the data was investigated by checking every data file for the channel number of the 511 keV gamma-ray. Comparing with the logbook, to see if the gain was changed manually on the amplifier, it was clear that the gain changed by itself several times during the experiment. Both in a continuos way and in sudden jumps. To remedy this it was necessary to perform several energy calibrations. For some files it was not possible to make a reliable energy calibration because the amplification were continuously drifting for some periods of time.

3.2 Efficiency calibration of the HPGe-detector

The experiment aims to determine the branching ratio of beta-delayed proton emission from ^{11}Be to the daughter nucleus ^{10}Be. Consequently it is necessary to measure the number of ^{11}Be atoms collected in the Cu plate and the number of ^{10}Be atoms in the Cu plate after all ^{11}Be nuclei have decayed. The number of ^{10}Be atoms is measured with the AMS technique at the University of Vienna. The number of ^{11}Be atoms collected in the Cu plate is determined from the decay spectrum measured with the HPGe-detector. From the decay scheme, Figure 2.3, it is clear that ^{11}Be beta-decays to excited states in ^{11}B, which decays by emission of gamma-rays that is measured.

It is necessary to understand the absolute efficiency of the detector as a function of energy, which is defined as the number of gamma-rays detected by the HPGe-detector relative to the total number of gamma-rays emitted by the source. The absolute efficiency depends on the position of the detector relative to the source because the solid angle is changing. Also, scattering and attenuation of the gamma-rays might be different in different detector positions. Therefore, it is important to place the sources used for the efficiency calibration in the exact same position, as where the Cu plate is placed, in order to have a reliable measure of the efficiency. If the sources are placed differently one need to correct for the changed position, which will introduce systematic uncertainties.

The three sources used for the efficiency calibration are the same as the sources used for the energy calibration, i.e. ^{60}Co, ^{152}Eu, and ^{228}Th (see Table 3.2 and Table 3.3). They were either positioned at the Cu plate position or attached to the Lead piece just in front of the HPGe-detector with the Lead piece between detector and source.

Determination of the absolute efficiency

For the calculation of the efficiency it is necessary to know the total number of decays from the source during the measurement time[1]. This number is given theoretically by the law of radioactive decay as

$$\#\text{decays} = N(t=0) - N(t) = N_0(1 - e^{-\lambda t}), \tag{3.1}$$

where λ is the decay constant. The number of nuclei, N_0, at the beginning of each measurement can be determined from the activity of the sources at the day of the experiment. It is given by the standard exponential decay curve and the reference activity, A_0, given in Table 3.2. An uncertainty on the activity of 2% is used according to the data sheets of the sources [9].

It is also necessary to know the total number of decays as seen by the detector. For this, fits to the best resolved gamma lines were done, using the fitting function given by

$$f(E) = p_0 + p_1 \cdot E + \int_{E_-}^{E_+} p_2 \cdot \frac{1}{\sqrt{2\pi} \cdot p_4} e^{-\left(\frac{E'-p_3}{p_4}\right)^2/2} \cdot dE' \tag{3.2}$$

$$= p_0 + p_1 \cdot E + p_2 \left[\text{Erf}\left(\frac{\left(E + \frac{p_5}{2}\right) - p_3}{p_4} \right) - \text{Erf}\left(\frac{\left(E - \frac{p_5}{2}\right) - p_3}{p_4} \right) \right] \tag{3.3}$$

where

$$\text{Erf}(x) = \frac{1}{\sqrt{2\pi}} \int_{-\infty}^{x} e^{-t^2/2} dt, \;\; x = \frac{E-\mu}{\sigma} \tag{3.4}$$

The background is estimated as a linear function with parameters p_0 and p_1. The peak is described with the HPGe-detector response function given by a normalized Gaussian distribution. The detector response function is integrated between E_- and E_+, where $E_+ - E_- = p_5$, for the number of counts in a certain bin of the histogram. The parameter p_2 is the area of the peak, p_3 is the centroid of the Gaussian distribution, p_4 is the standard deviation of the Gaussian distribution, and p_5 is the bin width of the histogram. This is a simplified parameterization of the line shape, however, as long as the same function is used for the efficiency calibration and the estimation of the number of atoms collected, the result should be consistent.

Finally it is also necessary to know the total gamma intensity of the gamma-rays used. These are given in Table 3.3 in per cent. The uncertainty on the gamma intensity is not used in the efficiency calculation as the activity and measurement time uncertainties dominates by far.

For the overall statistical uncertainty on the efficiency a simple estimate by the law of error propagation, without taking correlation terms into account, is used. The individual uncertainties that add up are coming from the activity, the measurement time, and the error on the fitting parameter p_2 (i.e. the peak area).

In conclusion the absolute efficiency is given, at the energy E_i of the gamma-rays used, by the following expression

$$\text{eff}(E_i) = \frac{(\text{number of counts in detector})}{(\text{total number of decays})} \left(\frac{\text{B.R.}_i}{100} \right)^{-1} \tag{3.5}$$

where the number of counts in the detector is given by the parameter p_2 in the fitting function in equation (3.3), the total number of decays is given by equation (3.1), and B.R.$_i$ is the gamma intensity in per cent given in Table 3.3. Using (3.5) the efficiency is given as a dimensionless fraction.

[1] A statistical uncertainty of 5s is conservatively assumed.

Table 3.2: *Data for the three sources used from [9].*

Source	Activity (Bq)	Date	RP ID	Halflife
^{60}Co	44500 ± 890	22$^{\text{nd}}$ of July 1996	3726RP	1925.28(14) d
^{152}Eu	37500 ± 750	12$^{\text{th}}$ of March 1996	3679RP	13.528(14) yr
^{228}Th	587.81 ± 11.76^a	5$^{\text{th}}$ of December 2012	4034RP	1.9116(16) yr

[a]No uncertainty is given for ^{228}Th but for both Co and Eu there is an uncertainty of 2% which I assume to be general, and therefore I also apply this to Th.

Table 3.3: *Energies and gamma intensities used for the three sources in the efficiency calibration. All data are found in [13].*

Source	Energy (keV)	Intensity (%)
^{60}Co	1173.228	99.85
	1332.492	99.9826
^{152}Eu	778.904	12.970
	964.079	14.605
	1085.869	10.207
	1112.074	13.644
	1408.006	20.850
^{228}Th	583.187	30.5
	727.330	6.67
	860.557	4.49
	1620.50	1.47
	2614.511	35.852

Following the above described steps results in Figure 3.2 for the absolute efficiency. The data exhibiting a high efficiency are for sources mounted at the lead piece in front of the HPGe-detector. The data exhibiting a low efficiency are with the source mounted in the Cu plate position. The data from the two positions clearly look consistent internally.

Corrections for different positions

The gamma-rays from the decay of ^{11}Be have energies of 2124keV and 2895keV. From Figure 3.2 it is clear that no measurement with the ^{228}Th source in the Cu plate position has been performed. However, the 2.615MeV gamma-ray from ^{228}Th is the only one with an energy above the ^{11}Be gamma-ray energy. To get the best possible description of the HPGe-detector efficiency in the ^{11}Be energy region it is necessary to have data points on both sides in energy. Consequently the next step is to correct the efficiencies measured with the source at the lead piece, so it corresponds to the source being in the Cu plate position. It is necessary to make two corrections: one for the attenuation in the Fe flange (a part of the vacuum chamber) and Cu plate, and another for the changing solid angle as seen by the detector.

The correction for the attenuation can be done in a simple manner described by the following formula

$$\frac{I}{I_0} = e^{-\mu(E)\cdot t} \tag{3.6}$$

where t is the thickness in units of g/cm^2 and μ is the mass attenuation coefficient in units of cm^2/g. The gamma-rays needs to pass through a thickness of 1.788g/cm^2 of Cu and

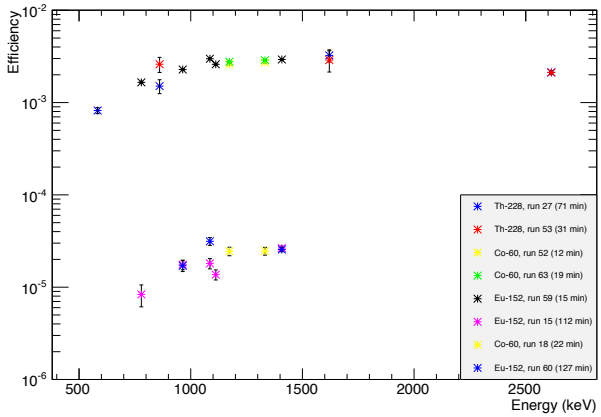

Figure 3.2: *Efficiency fraction versus energy in keV. The figure includes all efficiency data before any corrections are made. At the top are those with the source attached to the lead piece in front of the HPGe-detector. At the bottom are those with the source in the Cu plate position.*

9.42g/cm^2 of Fe. The mass attenuation coefficient was found in the reference table in [14] and its uncertainty was neglected in the calculation because the systematic error from the correction is believed to be larger. If the efficiencies, after correction for attenuation, follows the same trend as the efficiency data measured in the Cu plate position, they are assumed to be consistent.

Now lets look at the correction for the changing solid angle for which it is important to be aware of two things. First of all, the solid angle seen by the HPGe-detector depends on the energy of the gamma-ray, due to different path lengths inside the detector. Secondly, it is necessary to know the size of the HPGe-detector crystal and the exact position of the crystal inside the detector in order to determine the solid angle. Neither of these informations are known.

To take care of these unknowns in the best possible way measurements were performed with the ^{60}Co source in the Cu plate position and at the Lead piece. The ^{60}Co gamma-rays has a high signal-to-noise ratio, which makes them reliable for efficiency determination. By taking the ratio of the attenuation corrected efficiencies measured with the source at the Lead piece and the efficiencies measured in the Cu plate position gives a correction factor for the solid angle. A weighted average for the correction factor is made with the two gamma-rays from ^{60}Co. The weight used is given by $w_i = 1/\sigma_i^2$ where σ_i is the error on the correction factor for the individual gamma-rays.

As the correction will change with energy, this approach will introduce a systematic error, and the size of the error will change with energy. The result is the introduction of a larger spread in the efficiency data after the correction. But as the energy of the ^{60}Co gamma-rays is relatively close to the ^{11}B gamma-rays, the correction should describe the efficiency well in this region.

Resulting absolute efficiency function

Because the cross section for various photon interactions is described by power laws, it is possible to use the following fitting function

$$\varepsilon(E) = e^{p_0 + p_1 \cdot \ln(E)}, \tag{3.7}$$

to get the absolute efficiency as a function of energy.

It is important to note that the most reliable measurements of the absolute efficiency are the ones made with the source in the Cu plate position. Especially the ^{60}Co gamma-rays and the 2.614MeV gamma-ray from ^{228}Th are reliable for efficiency determination because of their large signal-to-noise ratio. Also, because the attenuation of gamma-rays mainly happens at low energy, the high energy ^{228}Th gamma-rays and the ^{60}Co gamma-rays are not influenced by this uncertainty.

A fit with equation (3.7) to the efficiency from the ^{60}Co and high-energy ^{228}Th gamma-rays can be seen on Figure 3.3. The following fitting parameters have been obtained:

$$p_0 = -8.42 \pm 0.64$$
$$p_1 = -0.31 \pm 0.09$$

The reason for not using more parameters is the low number of data points combined with the rather small energy dependence, which the data exhibit.

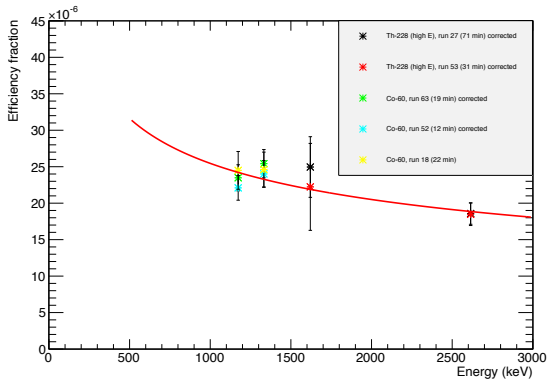

Figure 3.3: *Absolute efficiency fraction versus energy in keV. The figure shows the fit for the actual absolute efficiency calibration.*

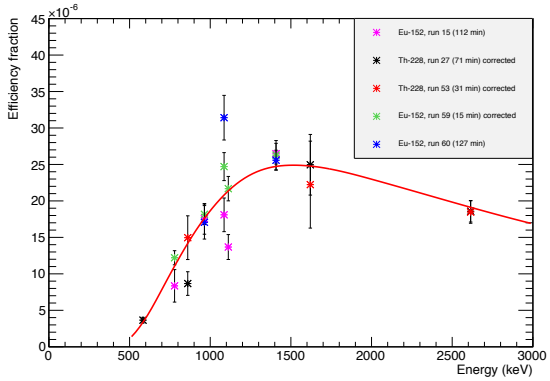

Figure 3.4: *Absolute efficiency fraction versus energy in keV. The fit to determine the systematic uncertainty for the absolute efficiency fraction data is shown.*

To get a measure of the systematic uncertainties a second fit was performed. The systematic uncertainties are mainly attributed to differences in the attenuation of gamma-

rays in the lead pieces. But other contributions are present as well. As the attenuation mainly happens for low energy gammas, it will be enough to look at gamma-rays from ^{152}Eu and ^{228}Th. The high energy ^{228}Th gamma-rays are included in order to get the correct functional behavior at large energies. To describe the physics of the attenuation correctly an absorption factor is introduced, similar to equation (3.6), which results in the following expression

$$\varepsilon(E) = e^{-\left(\frac{\mu(E)}{\rho}\right)\cdot\rho\cdot p_2} \times e^{p_0 + p_1\cdot\ln(E)} \tag{3.8}$$

Here μ is the mass attenuation coefficient for gammas in lead with units of cm^2/g and ρ is the density of lead. The data was found at [14].

A fit with this function can be seen at Figure 3.4 and the following fitting parameters are obtained:

$$p_0 = -0.27 \pm 1.14$$
$$p_1 = -1.13 \pm 0.14$$
$$p_2 = 3.50 \pm 0.25$$

Using the efficiency calibration in equation (3.7) with the parameters specified gives the following result for the efficiency at the two main gamma-ray energies from the beta-decay of ^{11}Be

$$\varepsilon(E = 2124\text{keV}) = 2.01(8)_{\text{stat}}(21)_{\text{sys}}\cdot 10^{-5} \tag{3.9}$$
$$\varepsilon(E = 2895\text{keV}) = 1.83(12)_{\text{stat}}(8)_{\text{sys}}\cdot 10^{-5} \tag{3.10}$$

The statistical uncertainty are coming from the fitting parameters in equation (3.7), and the systematic uncertainties are given by the difference between the two fits.

3.3 Number of ^{11}Be atoms collected

To get the number of collected ^{11}Be atoms a fit is performed to the 2124 keV and 2895 keV gamma lines with the function given in equation (3.3). Two gamma lines are used in order to get a consistency check of the efficiency calibration and of the data internally. An example of the decay spectrum can be seen at Figure 3.1. Here the 2124 keV gamma line is clearly seen along with the single and double escape lines. The 2895 keV gamma line is also seen, however, it is much less prominent. The decay scheme is shown in Figure 2.3.

To get the number of atoms collected, it is necessary to correct the number of counts in the HPGe-detector for several effects. First of all, a correction for the efficiency of the detector should be made. Second, as the amplification of the HPGe-detector changed by a factor of 2 during the experiment[2], it means that the 2895 keV gamma-ray was pushed outside the dynamic range of the detector for some time. Hence a correction for the period of time in which the 2895 keV gamma-ray was not visible in the detector should be made. Third, a correction for the detector dead time must be performed. The dead time is defined as the time after each recorded event in which the data acquisition system is busy recording the accepted event on the computer making it unable to record other events.

In order to correct for the missing data on the 2895 keV gamma-ray, it is necessary to look at how many 2124 keV gamma-rays are detected during the relevant time, compared to how many 2124 keV gamma-rays are detected in total. One minus the ratio between these two numbers should give a reliable estimate for the correction factor. The corresponding correction is 2.06%. This is only a correction to the 2895 keV gamma line.

In order to estimate how many decay events are lost because of the dead time of the HPGe-detector, it must be known that the data acquisition system saves the total number of

[2]See the section about the energy calibration.

events seen in the detector. However, only if the events are separated in time by at least the corresponding dead time of each event, is the detailed information of time and energy also saved to the computer. To determine the number of decay events lost in the complete collection time, the nature of the events happening in the dead time must be known. Looking at the total number of events between two consecutive accepted events and fitting it with a Poisson distribution, it is possible to determine if the events, that are not recorded, happens independently of each other. If they do happen independently, the events will be decay events.

It turns out that for the main part of the collection of ^{11}Be, the data follows a Poisson distribution. Therefore, the lost events happens independently of each other and are real decay events and not electronic noise. Hence it is sufficient to make a simple average by taking the ratio of the total number of accepted events to the total number of events. The resulting dead time correction is 2.82%.

The total amount collected is now given by the parameter for the area of the peak, p_2, divided by dead time, gamma-ray intensity, and efficiency, i.e.

$$\#^{11}\mathrm{Be}(E) = \frac{p_2}{(1 - DT) \cdot I_\gamma(E) \cdot \varepsilon(E)} \tag{3.11}$$

However, for the 2895keV gamma line it is also necessary to divide by $(1 - 0.0206)$ for the missing data.

Performing the calculation one gets the following result from each of the two gamma lines

$$\#^{11}\mathrm{Be}(2124\mathrm{keV}) = 1.377(34)_{\mathrm{stat}}(55)_{\mathrm{sys}} \cdot 10^{12} \tag{3.12}$$

$$\#^{11}\mathrm{Be}(2895\mathrm{keV}) = 1.538(65)_{\mathrm{stat}}(26)_{\mathrm{sys}} \cdot 10^{12} \tag{3.13}$$

The statistical uncertainties comes from p_2, the gamma-ray intensities, and the efficiency. For the systematic error there is only a contribution from the efficiency. For both systematic and statistical uncertainties no correlation terms have so far been considered.

Finally comes the combination of the two numbers into one by doing a weighted average with a proper description of the combination of errors. As one type of error does not dominate over the other, a proper treatment of both statistical and systematic errors are needed.

Assuming the two values for the number of atoms collected are fully correlated, it is possible to write

$$\mathrm{corr}(x, y) = \frac{\mathrm{cov}(x, y)}{\sigma_x \sigma_y} = \begin{pmatrix} 1 & \frac{\mathrm{cov}(x,y)}{\sigma_x \sigma_y} \\ \frac{\mathrm{cov}(y,x)}{\sigma_y \sigma_x} & 1 \end{pmatrix} \tag{3.14}$$

$$\Rightarrow \mathrm{cov}(x, y) = \begin{pmatrix} 34^2 + 55^2 & 55 \cdot 26 \\ 26 \cdot 55 & 65^2 + 26^2 \end{pmatrix} \tag{3.15}$$

using the fact that only systematic uncertainties will be in the off-diagonal elements. In the above the numbers are given in units of 10^9 atoms.

To calculate the weighted mean and the error on the weighted mean, equation (6.23) and (6.24) from [17] are used. They are given as

$$\hat{\mathbf{a}} = (\tilde{\mathbf{C}}\mathbf{V}(\mathbf{y})^{-\mathbf{1}}\mathbf{C})^{-\mathbf{1}}\tilde{\mathbf{C}}\mathbf{V}(\mathbf{y})^{-\mathbf{1}}\mathbf{y} \tag{3.16}$$

$$\mathbf{V}(\hat{\mathbf{a}}) = [\tilde{\mathbf{C}}\mathbf{V}(\mathbf{y})^{-\mathbf{1}}\mathbf{C}]^{-\mathbf{1}} \tag{3.17}$$

where $\mathbf{C} = \begin{pmatrix} 1 \\ 1 \end{pmatrix}$, $\tilde{\mathbf{C}} = \begin{pmatrix} 1 & 1 \end{pmatrix}$, $\mathbf{y} = \begin{pmatrix} 1377 \\ 1538 \end{pmatrix}$, and

$$\mathbf{V}(\mathbf{y}) = \mathrm{cov}(x, y) = \begin{pmatrix} 34^2 + 55^2 & 55 \cdot 26 \\ 26 \cdot 55 & 65^2 + 26^2 \end{pmatrix}. \tag{3.18}$$

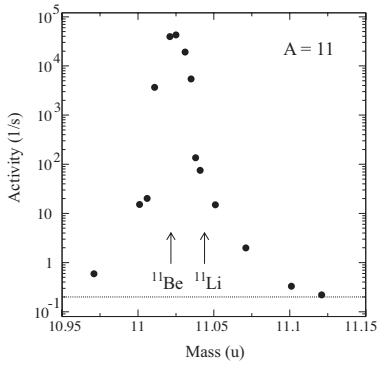

Figure 3.5: *Mass scan of the HRS across the ^{11}Be position. The beta activity measured is shown versus the mass with positions indicated for ^{11}Be and the possible background ^{11}Li. The horizontal line marks the detection limit of 0.2/s. Figure taken from [24].*

The final result is

$$\#^{11}\mathrm{Be} = \hat{\mathbf{a}} = 1.447(55) \cdot 10^{12} \tag{3.19}$$

number of ^{11}Be atoms collected in the Cu sample. The error is the combination of systematic and statistical uncertainties.

3.4 Beam background

To have a reliable measurement of the branching ratio of the βp decay mode, it is necessary to understand the beam background. Possible backgrounds could be ^{11}Li, which main decay branch βn also produces ^{10}Be, directly produced ^{10}Be, and directly produced ^{10}Be^{1}H molecules.

Mass profile of HRS

To understand the degree of contamination from the background, knowledge of the mass profile of the ISOLDE High Resolution Separator (HRS) is needed. The mass profile were determined by changing the mass settings of the HRS across the ^{11}Be mass position and measuring the beta activity in each step. The resulting mass profile can be seen on Figure 3.5. If the peak value for the ^{10}Be and ^{11}Li backgrounds are measured, it will give the complete knowledge of the mass profile for each of the two backgrounds, as the mass profile should be the same as for ^{11}Be.

^{11}Li background

During collection of ^{11}Be precautions were taken to reduce the amount of ^{11}Li implanted in the sample. First of all, by using the HRS mass separator to separate the ^{11}Li ion, which is displaced in mass with respect to ^{11}Be by $M/\Delta M = 500$. Second, by setting the beam gate to be closed in 150ms after proton impact on target, i.e. no beam is delivered to the setup for this period of time. As the half-life of ^{11}Li is 8.75ms, the main part of the ^{11}Li ions will have decayed by the time the beam gate is opened. The combined effect should be to suppress the ^{11}Li background by about 3 orders of magnitude as seen in an earlier experiment in 2001, [8].

However, to fully understand how large the contamination from ^{11}Li could be, a separate sample was collected for 80 minutes. The purpose of the sample is to estimate how much

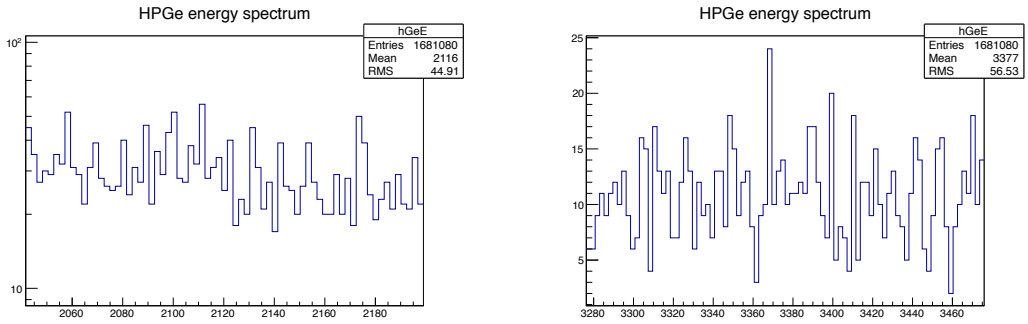

Figure 3.6: *HPGe energy spectrum in keV for the ^{11}Li collection. Left panel shows the region close to the 2124keV gamma line. Right panel shows the region close to the 3368keV gamma line. Both have 2.2 keV bin width.*

^{11}Li is produced directly in the peak of the mass profile. For this sample the HRS was set to the mass of ^{11}Li, and the beam gate was closed for 2ms after proton impact, after which it was open for 150ms. In this way long lived contamination was avoided. The lead shielding in front of the HPGe-detector was removed because low production rates were expected.

The gamma lines from ^{11}Li is measured with the HPGe-detector to estimate how much is collected. The two gamma lines used are the 2124keV (gamma intensity of 8%) and the 3368keV (gamma intensity of 33%). More information about the decay can be found in [16].

Looking at Figure 3.6, a closer look at the 2124keV and 3368keV gamma lines, it is clear that no signal is present above the background. For the 2124keV gamma line the number of counts is estimated to be 0 ± 34 before correcting for efficiency and branching. For the 3368keV gamma line the number of counts is estimated to be 0 ± 42 before corrections. Correcting for gamma intensity and efficiency[3] the following limits for the number of ^{11}Li atoms collected is achieved:

$$\#^{11}\text{Li}(2124\text{keV}) < 4.36 \cdot 10^6 \tag{3.20}$$

$$\#^{11}\text{Li}(3368\text{keV}) < 3.22 \cdot 10^6 \tag{3.21}$$

It is important to note that to get an upper limit on the number of atoms collected, the lowest possible efficiency should be used. I.e. the uncertainty on the efficiency have to be subtracted from the estimated absolute efficiency. An uncertainty of 30% on the efficiency have been used as an estimate.

^{10}Be background

To measure the production of ^{10}Be at the peak value of the mass profile for the HRS, a separate sample of ^{10}Be was taken for a period of 1 second with HRS set to the mass of ^{10}Be. By measuring the current on the Cu plate, it is estimated that $2.2 \cdot 10^7$ atoms (uncertain by a factor of two) were collected in this sample (see [24]).

^{10}Be^{1}H background

It is not possible to directly separate the ^{10}Be^{1}H^{+} molecular ions from the ^{11}Be ions as they are too close in mass ($M/\Delta M = 36600$). However, the molecule is unlikely to survive through the laser ion source as the ionization energy is 8.22 eV, which is much higher than

[3]Here was used the efficiency calculated at the experiment, as there was no lead piece in front of the HPGe-detector, and no off-line efficiency calibration without lead in front of the detector was made.

the dissociation energy of 3.26 eV, hence making it more likely to dissociate than to be ionized. To be completely certain of the amount of molecular background in the beam, data from an earlier experiment on ^{12}Be were checked for ^{11}Be^{1}H molecules. The upper limit found here corresponds to a ^{10}Be^{1}H intensity of less than $2 \cdot 10^{-6}$ of the ^{11}Be intensity (see [24]).

3.5 Resulting branching ratio

According to SRIM calculations ([19]) about 6% of all beryllium ions implanted in the Cu sample at an energy of 60 keV will backscatter out of the sample. Most of the backscattered ions are expected to remain close to the Cu plate so the gamma-rays from their decay will be seen, however, the decay products will not be in the Cu plate. This gives a correction, which is estimated to be $(4 \pm 4)\%$ ([24]).

Table 3.4: *Results of the AMS measurement. S1 to S3 denote the irradiated Cu samples (S1: ^{11}Be, S2: ^{11}Li, S3: ^{10}Be). 1st and 2nd correspond to the first or second leaching. Blank and S-blank are control samples without activity.*

Sample	^{10}Be/^{9}Be ratio	^{10}Be atoms
S1-1st	$(4.87 \pm 0.13) \cdot 10^{-13}$	$(1.17 \pm 0.05) \cdot 10^{7}$
S1-2nd	$(1.26 \pm 0.56) \cdot 10^{-15}$	$(3.03 \pm 1.35) \cdot 10^{4}$
S2-1st	$(3.10 \pm 0.94) \cdot 10^{-15}$	$(7.45 \pm 2.27) \cdot 10^{4}$
S2-2nd	$(4.4 \pm 3.1) \cdot 10^{-16}$	$(1.06 \pm 0.75) \cdot 10^{4}$
S3-1st	$(1.54 \pm 0.03) \cdot 10^{-12}$	$(3.70 \pm 0.13) \cdot 10^{7}$
S-blank	$(4.9 \pm 3.4) \cdot 10^{-16}$	$(1.18 \pm 0.82) \cdot 10^{4}$
blank	$(1.3 \pm 1.3) \cdot 10^{-16}$	$(3.12 \pm 3.12) \cdot 10^{3}$

The AMS measurement results are presented in Table 3.4. For samples S1 and S2 two leachings were performed with the values of the second leaching being consistent with the blank samples. This means that the implanted material were sitting in the surface, as expected, and not in the bulk of the samples. The number of atoms in sample S3 agrees with the estimated number from the current on the Cu plate. The lack of ^{10}Be atoms in the sample S2 is consistent with the lack of observed gamma-rays from the decay of ^{11}Li.

Looking at the mass profile for ^{11}Li, see Figure 3.5, and going down to the mass of ^{11}Be, it is clear that ^{11}Li is suppressed by 3 orders of magnitude relative to the peak value. Furthermore, from the AMS measurement of S2, correcting for a factor of 20 in different measurement times as compared to S1, a further suppression of at least a factor of 10 on the amount of ^{10}Be is achieved at the ^{11}Li mass as compared to the ^{11}Be mass (S1). Therefore in total maximum 1 out of 10^4 of the measured ^{10}Be atoms in sample S1 can be produced by the decay of ^{11}Li making it negligible.

As no gamma-rays are seen from the decay of ^{11}Li, the number of ^{10}Be atoms in S2 is a mixture of the tail from the directly produced ^{10}Be and of the decay of ^{11}Li. As stated above S2 limits the contamination from ^{11}Li to a negligible level, but it must also limit the directly produced ^{10}Be contamination to a negligible level.

The only remaining background in the beam, which could influence the measured number of ^{10}Be atoms in S1 is the ^{10}Be^{1}H molecules. But as stated the upper limit of $2 \cdot 10^{-6}$ on the intensity of ^{10}Be^{1}H as compared to the intensity of ^{11}Be is sufficient to rule out the molecular contamination.

A simple combination of the amount of ^{11}Be collected in S1 and the number of ^{10}Be atoms in S1, correcting for the backscattering effect, gives a branching ratio of $(8.4 \pm 0.6) \cdot 10^{-6}$.

4

Calibration and analysis of ^{20}Mg β-decay

In this chapter follows a description of the calibration and preliminary analysis performed for the beta-decay study of ^{20}Mg. In the first section the energy calibration procedure for all detectors is described. First is the geometry of the setup determined in order to understand the energy losses of the charged particles in the setup. Second is the energy calibration of the DSSSD detector described. Finally is the energy calibration procedure for the unsegmented detectors described.

In the second section follows a presentation of the preliminary analysis. Remember the motivation for this experiment is three-fold. First of all it is desired to study the almost complete charge independence of the nuclear force by comparison with the isospin mirror decay. Secondly, comparison of the beta-decay with modern Shell-Model calculations is desired. Finally the determination of the spin and parity of the 2.645(6)MeV resonance in ^{20}Na, either 1^+ or 3^+ from the mirror nucleus, is interesting for astrophysical reasons. In the first part of the preliminary analysis section is a short presentation of the analysis of the 2.645(6)MeV resonance. At the end is included a study of the beta-decay of ^{21}Mg, which was used as a calibration source of protons. It was not initially meant as an interesting physics case. But looking at the decay spectrum it was clear that a new beta-delayed alpha-particle branch was seen.

4.1 Calibration of detectors

As is well known charged particles will loose energy by electromagnetic interactions with the atomic electrons when traveling through a material. The thicker and denser the material is, the more energy is lost. Also the more charged the incoming particle is the more energy will it loose. E.g. will α-particles loose more energy than protons under otherwise similar conditions. The amount of energy lost is described by the SRIM stopping powers [19].

Table 4.1: *Dead layer and detector thicknesses.*

Detector	Thickness (μm)	Deadlayer (μm)[a]
Si1	300	$0.08 + 0.08$
Si2	500	0.08
Gas	7900	$7000 + 1500$
DSSSD	61	$0.1 + 0.8$
Epad	1498	0.760

[a] xx + yy meaning xx μm on frontside and yy μm on backside. If only xx it is just the frontside deadlayer.

Therefore, to calibrate the detectors and understand the measured energy of the charged particles, it is necessary to know the geometry of the experimental setup in terms of relative

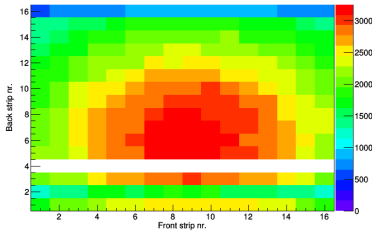

Figure 4.1: *Hit pattern of DSSSD from ^{21}Mg data. Back strip 2, 4, and 16 did not work properly as is clearly seen (horizontal lines). The color gives the number of counts in each pixel.*

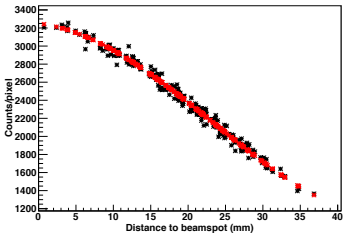

Figure 4.2: *Result of the fitting procedure. Red dots are the fitting polynomial, black dots are the pixels. It is the distance from the center of each pixel to (x_0, y_0) in millimeters.*

distances. I.e. the exact position where the implanted beam is stopped must be determined from measurements. Otherwise it is not possible to know the exact thickness of the materials that the particles will traverse, and it will not be possible to determine how much energy the particles will loose before they reach the detector. Therefore the first step in the energy calibration will be to determine the position of the implanted beam in the gas window. The geometry of the setup including the relative positions of some detectors were presented in figure 2.4 on page 9. Information on detector thickness and dead layer thickness are presented in Table 4.1.

When the geometry is known it is possible to energy calibrate the detectors by taking account of the energy losses. ^{21}Mg is used for proton calibration of the detectors. It decays by beta-delayed proton emission with well known proton energies making it a good calibration source. Because it is so close in mass to ^{20}Mg it can be guided through the ISOLDE beam lines by only changing the Q/M setting of the separator magnet. This ensures a similar implantation as for ^{20}Mg, and thereby minimizing systematic uncertainties.

Geometry calibration

To know the exact dead layer thickness, it is necessary to determine the position of the beam spot in the gas window. The position is determined from the hit-pattern of the DSSSD using the ^{21}Mg data, which is shown on Figure 4.1, assuming the beam spot is a point source. As the decay of ^{21}Mg has no preferred direction the emitted protons are expected to be uniformly distributed over 4π and the intensity distribution will directly give the beam spot position.

Defining a coordinate system with $(0,0)$ in the center of the DSSSD and the beam spot having the coordinates (x_0, y_0), geometrical considerations gives the distance from the beam spot to the center of any pixel, $|\vec{d}|$, as

$$\vec{d} = \vec{p} - \vec{r} = \begin{pmatrix} i \cdot (a+b) - c - x_0 \\ j \cdot (a+b) - c - y_0 \end{pmatrix} \tag{4.1}$$

where $c = \frac{49.5\text{mm}}{2} + \frac{a}{2} + b$[1], $\vec{p}$ is the vector from $(0,0)$ to the center of the pixel, $\vec{r}$ is the vector from $(0,0)$ to the beam spot, i is the front strip number, and j is the back strip number. $a = 3.0$ mm and $b = 0.1$ mm are respectively the strip width and the interstrip width.

The beam spot coordinates, (x_0, y_0), are found by fitting a 4th order polynomial to the number of hits in a pixel as a function of the distance, $|\vec{d}|$, from the beam spot to the

[1]The 49.5mm is the detector width given by 16 strip widths and 15 interstrip widths.

center of the pixel. The 4th order polynomial is given as a linear combination of orthogonal polynomials, which are defined in [18].[2]

Using a standard χ^2-minimization procedure and fitting to the intensity distribution shown on Figure 4.1, while excluding back strip 2, 4, and 16, produces the result shown on Figure 4.2 with the following parameter values

$$x_0 = 1.62\text{mm} \ , \ y_0 = -7.03\text{mm} \tag{4.2}$$

The error on the position are negligible as it is of the order 10^{-5}mm.

The assumption of a point source is not true as the beam will have a certain width when produced. However, the consequences of this assumption is not severe. For the x- and y-directions the centroid of the beam spot is found correctly. However, if the z-distance had been included in the fit the point source assumption produces a systematically larger value. But as the z-distance is already known to a sufficient accuracy from measurements of the chamber, it is not a problem.

Energy calibration of the DSSSD

As the position of the beam spot is determined, it is now possible to do the energy calibration with protons emitted from the beta-decay of ^{21}Mg. The data of the beta-decay are well known and can be used for a reliable proton calibration of the DSSSD. Assuming the daughter nucleus ^{21}Na* is at rest when emitting the protons, the proton energy can be determined from the Q-values of the proton emission, Q_p, and the mass of the daughter ^{20}Ne, as

$$E_p = Q_p \cdot \frac{M(^{20}Ne)}{M(^{20}Ne) + M_p} \tag{4.3}$$

The three most intense proton emissions are used, giving the proton energies 1252.0keV (7.47%), 1773.7keV (16.48%), and 1939.0keV (32.09%). The proton intensities are quoted as measured in [25].

For the calculation of energy losses of the protons the solid angle with respect to the source for each pixel must be known. It is given as

$$\Omega = \int\int_S \frac{\vec{R}\cdot\hat{n}}{R^3} dS = \int\int_S \frac{|\vec{R}|\cos\theta}{R^3} dS = \int\int_S \frac{\cos\theta}{R^2} dS \tag{4.4}$$

$$\approx \frac{\cos\theta}{R^2} \int\int_S dS = \frac{\cos\theta}{R^2} A(S) \tag{4.5}$$

where S is the smooth surface for which the solid angle is calculated, $\vec{R}$ is the vector from the source to the infinitesimal surface area dS, $\hat{n}$ is the normal vector of the infinitesimal surface dS, $A(S)$ is the area of the surface S, and θ is the angle between $\vec{R}$ and $\hat{n}$. Equation (4.5) is true if it is assumed that S, i.e. the pixel, is sufficiently far away from the source so that $\vec{R}$ does not change significantly when integrating over S.

Now the literature energies, given by equation (4.3), have to be corrected for energy losses in the gas window (0.0161μm polypropylene and 0.04μm Al for the shortest distance) and in the frontside dead layer of the DSSSD. The average energy loss of the protons in each strip of the DSSSD is calculated as the weighted average of the energy loss in all pixels covered by the strip. The weights are the solid angle of each pixel given by equation (4.5). The energy loss in each pixel is calculated assuming a constant dead layer thickness across the pixel,

[2]The coefficients in the linear combination are independent of each other, making the fit more robust, as there will be no correlation terms.

which is equal to the thickness in the center of the pixel. The SRIM stopping power tables are used, see [19].

The calibration is performed in two steps. First, a simple peak finding routine, which searches for the channel with the most counts, is used to find the centroid channel of the most intense peaks. The centroids are used in a preliminary linear calibration. Correcting the literature energy for the average energy loss in a strip, the preliminary calibration is used to convert this energy into a channel number. The channel numbers are used as a starting point in a more advanced fitting routine, taking into account the detector response function.

The advanced fitting function calculates the number of counts between ch_- and ch_+ (the difference $ch_+ - ch_-$ equals the bin width in the fitted histogram) from a normalized Gaussian response function on top of a linear background. The resulting function is

$$f(ch) = p_0 \cdot ch + p_1 + \frac{p_2}{2}\left[\mathrm{Erf}\left(\frac{ch_+ - p_3}{p_4 \cdot \sqrt{2}}\right) - \mathrm{Erf}\left(\frac{ch_- - p_3}{p_4 \cdot \sqrt{2}}\right)\right] \tag{4.6}$$

where p_0 is the slope of the linear background, p_1 is the offset of the linear background, p_2 is the peak area, p_3 is the centroid value, and p_4 is the standard Gaussian width σ. The function $\mathrm{Erf}(x)$ is defined in equation (3.4).

From the more advanced Gaussian fit, the parameter p_3 for the peak centroid and the uncertainty on p_3, is used in a final linear calibration that uses a standard χ^2-minimization procedure. This produces the desired final energy calibration of every strip in the DSSSD.

Energy calibration of unsegmented detectors

For the gas detector it was not possible to make an energy calibration. The problem is that the punch through energy, i.e. the energy above which the charged particles will pass through the detector, for protons is only 24 keV and for alpha particles is only 46 keV. It means that the decay spectrum will not exhibit any peaks making it very difficult to calibrate the detector.

For the detector called Si1 a calibration has been made using the ^{21}Mg proton source implanted in the gas detector window. The proton energies need to be corrected for energy losses in the gas window (1.06μm), in the gas (16.4mm), and in the frontside dead layer of the Si1 detector (0.08μm). The distances quoted are the shortest possible distances from source to detector. As the detector is unsegmented an expression for the energy loss averaged over all angles covering the detector has to be made to get a more accurate calibration. The average weighted energy loss is given by

$$< E_{\mathrm{loss}} >= \frac{\int_0^{2\pi}\int_0^{\theta_{\max}} E_{\mathrm{loss}}(\theta)\frac{\mathrm{d}\Omega}{\Omega_{\mathrm{det}}}}{\int_0^{2\pi}\int_0^{\theta_{\max}}\frac{\mathrm{d}\Omega}{\Omega_{\mathrm{det}}}} = \frac{\int_0^{\theta_{\max}} E_{\mathrm{loss}}(\theta)\sin\theta\mathrm{d}\theta}{\int_0^{\theta_{\max}}\sin\theta\mathrm{d}\theta} \tag{4.7}$$

where $\mathrm{d}\Omega = \sin\theta\mathrm{d}\theta\mathrm{d}\phi$ is an infinitesimal solid angle, Ω_{det} is the total solid angle of the detector, and $\mathrm{d}\Omega/\Omega_{\mathrm{det}}$ is the weights of each circular disc.

For small angles, θ, it may be assumed that $E_{\mathrm{loss}}(\theta) \approx \frac{E_{\mathrm{loss}}(\theta=0)}{\cos\theta}$, i.e. assuming the energy loss is proportional to the length travelled. The final result for the averaged energy loss becomes

$$< E_{\mathrm{loss}} >\approx E_{\mathrm{loss}}(\theta=0)\frac{\int_0^{\theta_{\max}}\tan\theta\mathrm{d}\theta}{\int_0^{\theta_{\max}}\sin\theta\mathrm{d}\theta} = E_{\mathrm{loss}}(\theta=0)\frac{-\ln(|\cos\theta_{\max}|)}{1-\cos\theta_{\max}} \tag{4.8}$$

Using the ^{21}Mg proton energies 1773.7 keV (16.48%), 1939.0 keV (32.09%), and 4675 keV (4.78%) and correcting for the average weighted energy loss given by equation (4.8), the following calibration of the Si1 detector is obtained,

$$E(ch) = 1.421(6) \cdot ch - 35.6(1.3) \tag{4.9}$$

For the Si2 detector, as for the gas detector, a calibration were not feasible. Again we do not need an exact knowledge of the energy scale here, as the main particles of interest will be stopped in the Si1 detector, which have punch through energies of 6.0MeV for protons and 24.2MeV for alpha particles. The Si2 detector is mainly used as a veto in the analysis to remove β-particles, which much easier punch through the Si1 detector.

The final calibration for the pad detector is not yet ready.

4.2 Preliminary analysis

Here follows a description of the analysis work performed so far. The analysis is only preliminary, and mainly included to show the possibilities of the data. First, is a short description of the analysis of the 2.645(6)MeV. Second, is an investigation of the beta-decay of ^{21}Mg presented focusing on the new $\beta\alpha$ branch.

Spin and parity of the 2.645(6)MeV resonance in ^{20}Na

To determine the spin and parity of the 2.645(6) MeV resonance in ^{20}Na, the beta feeding for the resonance needs to be determined. If the beta feeding is known, it is possible to translate it into a degree of forbiddenness of the beta-decay and using the selection rules described in chapter 2.1, the spin and parity can be determined. As the possible spin and parity are either 1^+ or 3^+, the beta-decay from the 1^+ ground state of ^{20}Mg must either be an allowed or a second-forbidden transition, respectively.

It is possible to determine the beta feeding by measuring the emitted protons from the resonance. To determine the energy of the proton equation (4.3), with the mass of ^{19}Ne replacing the mass of ^{20}Ne, can be used. It gives a kinetic energy of the emitted protons of 427(8)keV. Correcting for energy losses in the gas window, the gas, and the Si1 dead layer, gives an energy of the proton in the Si1 detector of about 366keV. Knowing the energy of the proton the next step is to look for it.

Remember that alpha-particles in general deposit more energy in a given material than protons do under similar conditions. Then it is clear from Figure 4.3 that the Si1 energy spectrum includes intense $\beta\alpha$ branches at large values of ch_{gas}, and several βp branches at low ch_{gas} values. At low energy in Si1 a huge amount of counts is present being both beta-particles, protons, and heavier particles like recoiling daughter nuclei. The huge number of counts at low energy are clearly seen on Figure 4.4, where the blue curve is the complete decay spectrum in Si1, without any demands on the individual events.

By demanding that $100 < ch_{gas} < 1000$ should remove most of the heavy particles, leaving mainly protons and beta-particles in the spectrum. This is the red curve on Figure 4.4 and it is seen to remove the two intense $\beta\alpha$ branches close to 2.0MeV and to reduce the number of counts in the high energy $\beta\alpha$ branches.

Further demanding that $E_{\mathrm{Si2}} = 0$ and $E_{\mathrm{pad}} > 0$ should remove many of the low energy events coming from beta-particles. This is the green curve on Figure 4.4 and it clearly removes many of the low energy events. As it is mainly expected to be very high energy protons or beta-particles that punch through the Si1 detector and hits Si2, demanding that $E_{\mathrm{Si2}} = 0$ will remove many undesired events that potentially could deposit an energy in Si1 similar to the 366keV of the proton. Requiring a signal in the Pad detector should minimize the probability of having a beta-particle in Si1, but it could also be a high energy proton that is detected in the Pad detector.

However, no sign of the 366keV protons is present. Further analysis is needed.

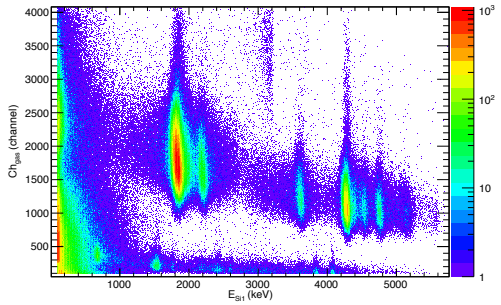

Figure 4.3: *Energy of the Si1 detector on the x-axis and channel number in the gas counter on the y-axis for the ^{20}Mg data. The color coding gives the number of counts.*

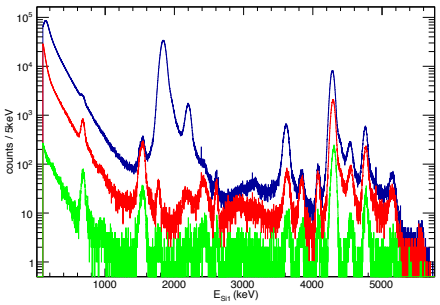

Figure 4.4: *Decay spectrum of the ^{20}Mg beta-decay in Si1. The blue curve is the full spectrum. The red and green curves are the decay spectrum with two different cuts.*

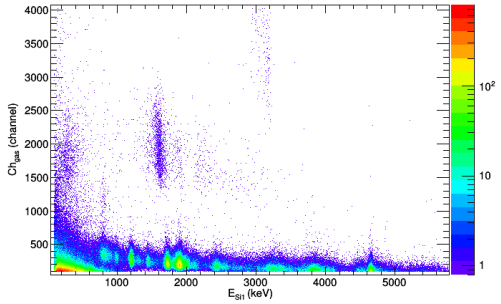

Figure 4.5: *Energy of Si1 detector on the x-axis and channel in the gas counter on the y-axis for the ^{21}Mg data. The color coding gives the number of counts.*

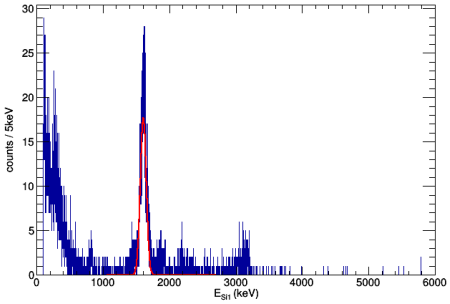

Figure 4.6: *Energy spectrum of ^{21}Mg beta-decay in the Si1 detector gated on $ch_{gas} >$ 1000 in order to cut away the protons. A Gaussian fit to the peak is shown.*

Beta-delayed alpha emission from ^{21}Mg

The data on ^{21}Mg were intended as a well-known proton source for the calibration. However, by investigating the data a new decay mode has been identified. Looking at Figure 4.5 the main part of the events are seen to be below channel 1000 in the gas detector, while a few events are seen to deposit significantly more energy. Knowing that the stopping power of protons is lower than for alpha-particles, it is possible to identify the events in the region $3000 > ch_{\text{gas}} > 1500$ and $E_{\text{Si1}} \approx 1600$ keV as alpha particles. Gating on the gas detector such that $ch_{\text{gas}} > 1000$ should remove most of the protons from the energy spectrum of the Si1 detector. This is shown on Figure 4.6 together with a Gauss fit to the main peak giving a centroid energy of 1609.4 keV. Going backwards and correcting for energy losses in dead layers and making the angular correction of equation (4.8) gives an emitted energy of 1960.04 keV of the alpha-particle.

The alpha-particles might be emitted from either ^{21}Na or ^{21}Ne (stable). However, from [26] it is clear that the beta-decay of ^{21}Na to ^{21}Ne populates excited states up to 2.8 MeV and as $Q_\alpha = -7347.88$ keV ([26]) it is energetically not allowed to emit alpha-particles from ^{21}Ne. The alpha-particles must be emitted from ^{21}Na. Indeed the beta-decay of ^{21}Mg does populate resonances above the ^{17}F+α threshold at 6560 keV above the ground state of ^{21}Na,

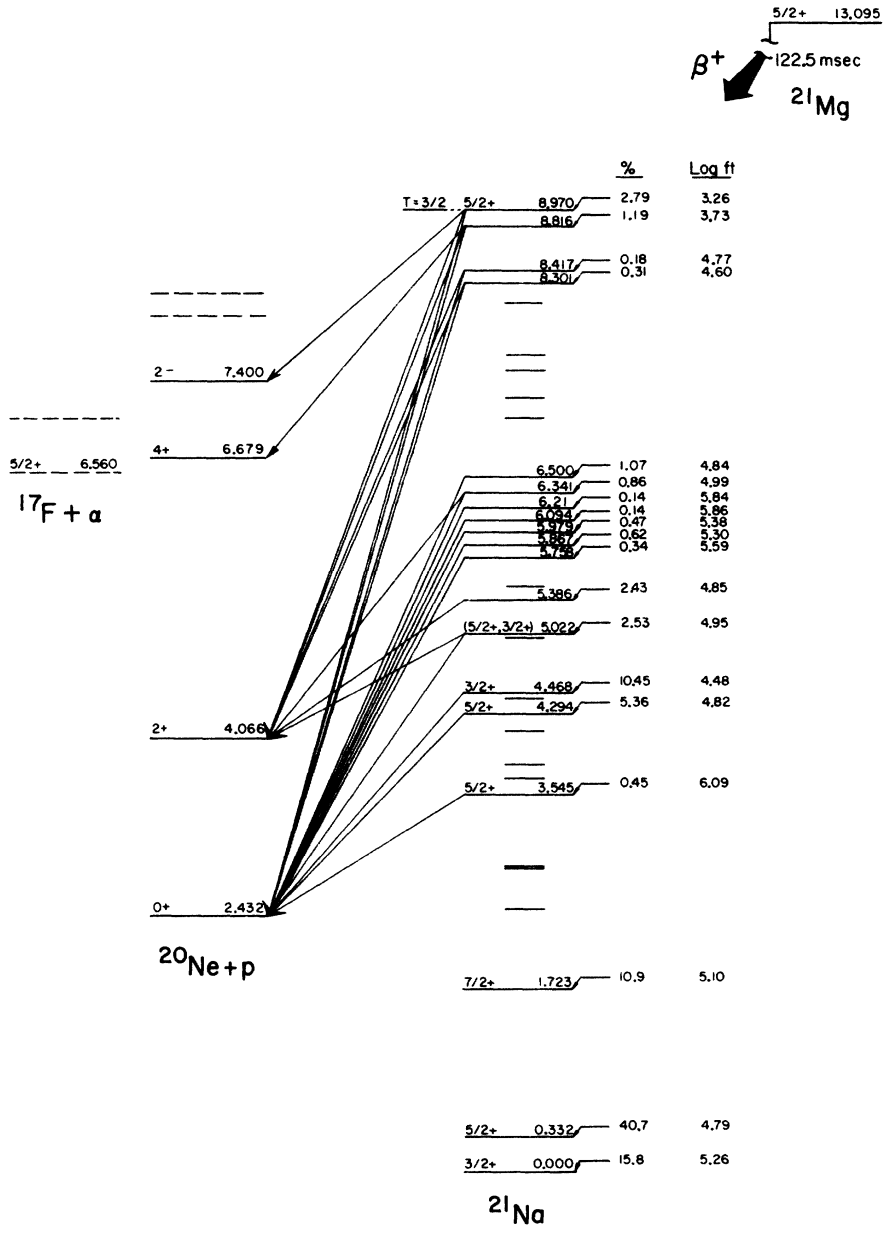

Figure 4.7: *Decay scheme of the beta-decay of* ^{21}Mg*. As given by [25].*

see Figure 4.7.

Using the inferred kinetic energy of the alpha-particle, the Q-value can be determined as

$$Q_\alpha = E_\alpha \cdot \frac{M(^{17}F) + M_\alpha}{M(^{17}F)} = 2421.34\text{keV} \tag{4.10}$$

using $M(^{17}F) = 17.0021$ a.m.u. and $M(\alpha) = 4.0015$ a.m.u. The Q-value corresponds to alpha emission from the ^{21}Na resonance at 8.970 MeV and going to the ground state of ^{17}F at 6.560 MeV.

5

Outlook

In this chapter a short outlook of the ^{11}Be and ^{20}Mg beta-decay studies will be presented. Finally we have plans for a future study of the beta-decay of ^{20}F, which will be presented with a short motivation and a description of the proposed experiment.

5.1 Beta-delayed proton emission from ^{11}Be

The measured value for the branching ratio of beta-delayed proton emission from ^{11}Be, $B_{\beta p} = (8.4 \pm 0.6) \cdot 10^{-6}$, is a factor of 100 higher than predicted by theory. This calls for a new experiment to confirm the measurement. In the original experiment we had many technical problems with producing the required ^{11}Be beam, so we did not have enough time to take more than one sample of ^{11}Be or to make as thorough checks of the beam composition as we had hoped. We would have liked to use 24h on taking a sample on the mass of ^{11}Be but without RILIS, as a check for ^{10}Be^{1}H molecules. As it is now, we only have a limit on the production rate of this molecule inferred from another experiment. In a future experiment we would like to take one or two new sources of ^{11}Be, one source on the mass of ^{11}Be but without RILIS to check for molecular ions, and one source of ^{11}Li taken over longer time to increase the statistics.

Theoretical calculations have been performed with the basic assumption that the beta-decay happens as an essentially detached decay of the halo neutron into a proton. The conclusion is that the large measured branching ratio must be due to an unseen resonance in ^{11}B, through which the decay will go (see [24]). As this claimed resonance has never been seen before, preparations are being made, to perform proton scattering on a ^{10}Be target at the local 400 keV Van de Graaf accelerator to look for the resonance. By measuring the cross section for proton scattering on ^{10}Be as a function of energy it should be possible to search for the new resonance.

5.2 Beta-decay study of ^{20}Mg

At the present moment I am working on finalizing the calibrations, and hope to start the in depth analysis of the data soon. For the analysis we need to search for the 450keV proton from the 2.645(6)MeV level in ^{20}Na, to put limits on the beta-intensity to this resonance, and hopefully clarify if it is a 1^+ or 3^+ resonance. Further investigation is also needed to establish the level scheme of ^{20}Na and a comparison with a Shell-Model calculation is on the to do list.

In the calibration data of ^{21}Mg we need to investigate the new alpha-emission branch. It is the first evidence for beta-delayed alpha-particle emission from ^{21}Mg. The parent resonance of the alpha-particle is believed to be the 8.970MeV resonance (isospin $T = \frac{3}{2}$) of ^{21}Na. This is the isobaric analog state (IAS) of the ground state of ^{21}Mg, which makes the

new $\beta\alpha$ branch interesting for isospin-mixing studies of the 8.970MeV resonance, i.e. is it a pure isospin $\frac{3}{2}$ state.

It could also be interesting to look for more alpha-emission branches in the data, and to search for the recoiling daughter nucleus, ^{17}F. We should be able to get more statistics on the alpha decay branch if we search for the decay mode in the DSSSD side of the setup.

At the present moment only part of the beam time attributed at ISOLDE has been used. In the near future, hopefully in the fall of 2014, a new experiment is planned to use the new ISOLDE decay station with both charged particle and gamma detection ([27]). Such an experiment should hopefully give much more statistics on the beta-decay, and direct detection of the 450 keV proton is hopefully possible.

5.3 Beta-decay study of ^{20}F

The stellar mass range of $8 \leq M/M_{\odot} \leq 12$ is host to the most massive AGB stars, the super-AGB stars, with masses up to $10M_{\odot}$, but also to more massive stars. Many of the supernovae progenitors are also found here, and it is therefore a very important region to understand in terms of nucleosynthesis, as the stars contribute heavily to the galactic chemical evolution ([21]).

A recent study, [21], of stellar evolution in this mass range, find that an inward propagating neon-oxygen burning shell is common to both the lowest mass Fe core-collapse supernovae progenitors and the most massive electron capture supernovae (EC-SN) progenitors (both with $M \approx 9M_{\odot}$, see [21]). For an $8.8M_{\odot}$ model a Ne burning shell develops but fails to propagate entirely to the center of the core, due to the fact that an extended region of low electron number density develops in the outer part of the core in the late evolution due to electron captures. The model will end in an EC-SN, i.e. the removal of electrons from the core by electron captures will make it unstable and eventually causing it to collapse, resulting in a supernova explosion. This is a completely new progenitor for the EC-SN, which usually is a super-AGB star going through the thermal pulsing phase until electron capture reactions remove the electron pressure.

The new EC-SN progenitor model described here is quite sensitive to the exact electron capture rate on ^{20}Ne, as the threshold density for the onset of this reaction could change, making the model end up in a completely different scenario. Hence, a measurement of the electron capture rate on ^{20}Ne is particularly important [20].

Measuring the rate of electron capture on ^{20}Ne is equivalent to measuring the beta-decay rate of ^{20}F, as the two rates at a fixed energy are related by the phase space available in the exit channel (see chapter 2 of [23]). The decay scheme of ^{20}F can be seen on Figure 5.1 together with the measured beta intensities. It is clear that the decay is dominated by the allowed beta-decay to the first excited 2^+ state in ^{20}Ne, $I_{\beta} = 99.9913\%$. However, in the stellar environment of the progenitor the temperature is not sufficiently high to populate the first excited state of ^{20}Ne[1]. A measurement of the second-forbidden beta-decay from ground state to ground state is needed. However, as the decay is second-forbidden it is strongly suppressed as compared with the allowed transition and only an upper limit on the beta intensity exist, measured by Calvin Wong in 1954 (see [22]).

The best way to measure the second-forbidden transition will be to measure the beta-particle energy spectrum. The spectrum will be dominated by the allowed decay going to the first excited state, with a beta spectrum endpoint at $(7.02 - 1.63)$MeV$= 5.39$MeV. The second-forbidden transition, however, has a larger energy available, 7.02MeV, giving rise to a small high-energy tail on the allowed beta-decay spectrum. If beta particles are detected with an energy greater than the 5.39MeV, it is for sure from the second-forbidden decay.

[1] At the ignition of Ne-burning the temperature corresponds to roughly 110keV.

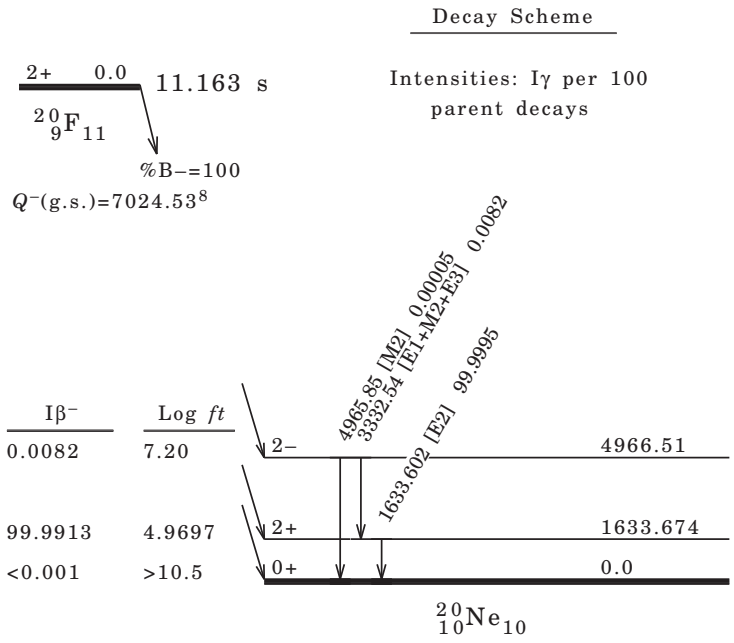

Figure 5.1: *Decay scheme of the beta-decay of* ^{20}F*. Taken from [20].*

The only problem is to distinguish these high-energy beta-particles from pile-up signals, i.e. two low-energy beta-particles in the same trigger window summing their energy.

We would like to measure the beta-particles with a LEGe (Low Energy Ge, [28]) detector with a Be window or with a scintillator. We also want to measure the gamma-rays with a standard HPGe-detector. Then it is possible to gate on events with no gamma-ray signals. This cut will exclude most of the beta-decays to excited states in ^{20}Ne. However, as we will have dead time and a limited solid angle coverage, some beta-decays to excited states will survive the cut, so pile-up events might still be present. To make sure the signal is not a pile-up event, we want to do digital data acquisition in order to store the traces of all events, i.e. the entire pulse shape of the signal in each individual trigger window. This should be sufficient to distinguish between pile-up events and real single beta-particle events.

The location we have in mind for the experiment is the IGISOL facility in Jyväskula, Finland. The facility should easily be able to deliver 10^4 ^{20}F atoms/s in a ^{19}F(d, p) reaction. If two weeks of beam time is granted we can potentially produce $1.2 \cdot 10^{10}$ ^{20}F atoms and measure their beta-decay. This kind of statistics is more than sufficient to at least determine a much better upper limit on the second-forbidden beta-decay intensity to the ground state of ^{20}Ne.

Bibliography

[1] E. Rutherford, *The Scattering of α and β Particles by Matter and the Structure of the Atom*, Philosophical Magazine. Series 6, vol. 21. May 1911

[2] Petr Navrátil, Sofia Quaglioni, Ionel Stetcu and Bruce R Barrett, *Recent developments in no-core shell-model calculations*, J. Phys. G: Nucl. Part. Phys. 36 (2009) 083101

[3] Michael S. Smith and K. Ernst Rehm, *Nuclear astrophysics measurements with radioactive beams*, Annual Review of Nuclear and Particle Science vol. 51, 91-130.

[4] M.J.G. Borge, J. Cederkäll, L.M. Fraile, H.O.U. Fynbo, T. Giles, K.L. Jensen, J.S. Johansen, B. Jonson, G.T. Koldste, E. Nacher, T. Nilsson, A. Perea, K. Riisager, T. Storra, O. Tengblad, *Study of the β-decay of ^{20}Mg*, Proposal to the INTC, INTC-P-285

[5] Alain Coc, *Nucleosynthesis in novae: experimental progress in the determination of nuclear reaction rates*, arXiv:0801.2923 [astro-ph]

[6] B. Jonson and K. Riisager, *Beta-decay of exotic nuclei*, Nucl.Phys. A693 (2001) 77

[7] D. Baye and E.M. Tursonov, *β delayed emission of a proton by a one-neutron halo nucleus*, Phys.Lett. B696 (2011) 464

[8] A. Becerril, M.J.G. Borge, J.A. Briz, O. Forstner, L.M. Fraile, H.O.U. Fynbo, J.S. Johansen, B. Jonson, G.T. Koldste, K.L. Laursen, M.V. Lund, T. Nilsson, G. Nyman, K. Riisager, P. Steier, O. Tengblad, *Search for beta-delayed protons from ^{11}Be*, Proposal to the INTC, INTC-P-331

[9] `http://www.cern.ch/rp`

[10] J.P. Wallace, P.J. Woods, G. Lotay, A. Alharbi, A. Banu, H.M. David, T. Davinson, M. McCleskey, B.T. Roeder, E. Simmons, A. Spiridon, L. Trache, R.E. Tribble, *β-Delayed proton-decay study of ^{20}Mg and its implications for the $^{19}Ne(p, \gamma)^{20}Na$ breakout reaction in X-ray bursts*, Physics Letters B 712 (2012) 59-62

[11] S. Rothe, B.A. Marsh, C. Mattolat, V.N. Fedosseev and K. Wendt, *A complementary laser system for ISOLDE RILIS*, Journal of Physics: Conference Series 312 (2011) 052020

[12] A.S. Jensen, P.J. Siemens, *Elements of nuclei*, Addison Wesley, 1987

[13] `http://www.nndc.bnl.gov`

[14] `http://www.nist.gov/pml/data/xraycoef/`

[15] M.J.G. Borge, L.M. Fraile, H.O.U. Fynbo, B. Jonson, O.S. Kirsebom, T. Nilsson, G. Nyman, G. Possnert, K. Riisager, O. Tengblad, *Rare βp decays in light nuclei*, J. Phys. G: Nucl. Part. Phys. 40 035109 (2013)

[16] H.O.U. Fynbo, M.J.G. Borge, J. Cederkäll, S. Courtin, P. Dessagne, B. Jonson, G. Le Scornet, T. Nilsson, G. Nyman, E. Poirier, K. Riisager, O. Tengblad, K. Wilhelmsen, ISOLDE Collaboration, *New information on the β-decay of ^{11}Li from Doppler broadened γ lines*, Nuclear Physics A 736 (2004)

[17] R. J. Barlow, *Statistics: A Guide to the Use of Statistical Methods in the Physical Sciences*

[18] R. J. Barlow, *SLUO Lectures on Statistics and Numerical Methods in HEP. Lecture 7: Fitting Methods.*

[19] J.F. Ziegler, Particle interactions with matter. `http://www.srim.org`

[20] Gabriel Martínez Pinedo, *Exotic nuclei and explosive nucleosynthesis*, presentation at the ISOLDE workshop and users meeting 2013.

[21] S. Jones, R. Hirschi, K. Nomoto, T. Fischer, F.X. Timmes, F. Herwig, B. Paxton, H. Toki, T. Suzuki, G. Martínez-Pinedo, Y.H. Lam, M.G. Bertolli, *Advanced burning stages and fate of 8-10$M_\odot$ stars*, 2013 ApJ **772** 150.

[22] Calvin Wong, *Beta Decay of F^{20}*, Physical Review vol. 95 number 3, 1954.

[23] C. Iliadis, *Nuclear Physics of Stars*, Wiley-VCH, 2007

[24] K. Riisager, O. Forstner, M.J.G. Borge, J.A. Briz, M. Carmona-Gallardo, L.M. Fraile, H.O.U. Fynbo, T. Giles, A. Gottberg, A. Heinz, J.G. Johansen, B. Jonson, J. Kurcewicz, M.V. Lund, T. Nilsson, G. Nyman, E. Rapisarda, P. Steier, O. Tengblad, R. Thies, S.R. Winkler, *Quasi-free neutron decay in the periphery of a nucleus*, submitted to Nature Physics.

[25] Richard G. Sextro, R. A. Gough, Joseph Cerny, *β^+-Delayed-Proton Decay of ^{21}Mg.*, Phys. Rev. C 8, 258-268 (1973)

[26] R.B. Firestone, *Nuclear Data Sheets for A=21*, Nuclear Data Sheets, Volume 103, Issue 2, October 2004, Pages 269-324.

[27] `http://isolde.web.cern.ch/sites/isolde.web.cern.ch/files/P_Van-Duppen.pptx`

[28] J. Huikari, M. Oinonen, A. Algora, J. Cederkäll, S. Courtin, P. Dessagne, L. Fraile, S. Franchoo, H. Fynbo, W.X. Huang, A. Jokinen, A. Knipper, F. Marechal, C. Miehé , E. Nacher, K. Peräjärvi, E. Poirier, L. Weissman, J. Äystö, and the ISOLDE Collaboration, *Mirror decay of ^{75}Sr*, Eur. Phys. J. A 16, 359-363 (2003)